Danilovich T., Ramstedt S., Gobrecht D., Decin L., De Beck E., Olofsson H., 2018, A&A, 617, A132
Danilovich T., Richards A. M. S., Karakas A. I., Van de Sande M., Decin L., De Ceuster F., 2019, MNRAS, 484, 494
Danilovich T., Richards A. M. S., Decin L., Van de Sande M., Gottlieb C. A., 2020, MNRAS, 494, 1323
Danilovich T. et al., 2021, A&A, 655, A80
Danilovich T. et al., 2024, Nat. Astron., 8, 308
De Beck E., Decin L., de Koter A., Justtanont K., Verhoelst T., Kemper F., Menten K. M., 2010, A&A, 523, A18
Decin L. et al., 2016, A&A, 592, A76
Decin L. et al., 2019, Nat. Astron., 3, 408
Decin L. et al., 2020, Science, 369, 1497
Decin L., Richards A. M. S., Danilovich T., Homan W., Nuth J. A., 2018, A&A, 615, A28
Delfosse X., Kahane C., Forveille T., 1997, A&A, 320, 249
Engels D., Etoka S., Gérard E., Richards A., 2015, in Kerschbaum F., Wing R. F., Hron J.eds, ASP Conf. Ser. Vol. 497, Why Galaxies Care about AGB Stars III: A Closer Look in Space and Time. Astron. Soc. Pac., San Francisco, p. 473
Engels D., Etoka S., Jiménez-Esteban F., Herrmann W., López-Martí B., 2024, in de Grijs R., Whitelock P. A., Catelan M.eds, IAU Symp. Vol. 376, p. 328
Freytag B., Höfner S., 2023, A&A, 669, A155
Ginsburg A., McGuire B., Plambeck R., Bally J., Goddi C., Wright M., 2019, ApJ, 872, 54
Ginsburg A. et al., 2023, ApJ, 942, 66
Gottlieb C. A., Myers P. C., Thaddeus P., 2003, ApJ, 588, 655
Gottlieb C. A. et al., 2022, A&A, 660, A94
Güsten R., Nyman L. Å., Schilke P., Menten K., Cesarsky C., Booth R., 2006, A&A, 454, L13
Harris C. R. et al., 2020, Nature, 585, 357
Helmer M., Plane J. M. C., 1993, J. Chem. Phys., 99, 7696
Helou G., Walker D. W.eds, 1988, Infrared Astronomical Satellite (IRAS) Catalogs and Atlases,Vol. 7: The Small Scale Structure Catalog.https://cdsarc.cds.unistra.fr/viz-bin/cat/II/125
Herwig F., 2005, ARA&A, 43, 435
Heske A., Forveille T., Omont A., van der Veen W. E. C. J., Habing H. J., 1990, A&A, 239, 173
Highberger J. L., Thomson K. J., Young P. A., Arnett D., Ziurys L. M., 2003, ApJ, 593, 393
Hoang T. D., Karska A., Lee M. Y., Wyrowski F., Tram L. N., Yang A., Menten K. M., 2023, A&A, 679, A121
Hunter J. D., 2007, Comput. Sci. Eng., 9, 90
Husain D., Marshall P., 1986, Int. J. Chem. Kinetics, 18, 83
Irvine W. M., Senay M., Lovell A. J., Matthews H. E., McGonagle D., Meier R., 2000, Icarus, 143, 412
Justtanont K. et al., 2015, A&A, 578, A115
Justtanont K., Olofsson G., Dijkstra C., Meyer A. W., 2006, A&A, 450, 1051
Justtanont K., Teyssier D., Barlow M. J., Matsuura M., Swinyard B., Waters L. B. F. M., Yates J., 2013, A&A, 556, A101
Justtanont K., Tielens A. G. G. M., 1992, ApJ, 389, 400
Juvela M. et al., 2015, A&A, 584, A94
Kamiński T., Gottlieb C. A., Young K. H., Menten K. M., Patel N. A., 2013, ApJS, 209, 38
Karakas A. I., Lattanzio J. C., 2014, Publ. Astron. Soc. Aust., 31, e030
Karakas A. I., Lugaro M., 2016, ApJ, 825, 26
Kessler M. F. et al., 1996, A&A, 315, L27
Khouri T. et al., 2014, A&A, 561, A5
Kim H., Trejo A., Liu S.-Y., Sahai R., Taam R. E., Morris M. R., Hirano N., Hsieh I. T., 2017, Nat. Astron., 1, 0060
Klisch E., Schilke P., Belov S. P., Winnewisser G., 1997, J. Mol. Spectrosc., 186, 314
Kuan Y.-J., Mehringer D. M., Snyder L. E., 1996, ApJ, 459, 619
Lee S. K., Ozeki H., Saito S., 1995, ApJS, 98, 351
Lindqvist M., Nyman L.-A., Olofsson H., Winnberg A., 1988, A&A, 205, L15
Mamon G. A., Glassgold A. E., Huggins P. J., 1988, ApJ, 328, 797
Marigo P. et al., 2020, Nat. Astron., 4, 1102
Marini E. et al., 2023, A&A, 670, A97
Martín S., Mauersberger R., Martín-Pintado J., García-Burillo S., Henkel C., 2003, A&A, 411, L465
Martín S. et al., 2021, A&A, 656, A46
Massalkhi S., Agúndez M., Cernicharo J., 2019, A&A, 628, A62
McGonagle D., Irvine W. M., 1997, ApJ, 477, 711
Milam S. N., Apponi A. J., Woolf N. J., Ziurys L. M., 2007, ApJ, 668, L131
Millar T. J., Herbst E., 1990, A&A, 231, 466
Moe M., Di Stefano R., 2017, ApJS, 230, 15
Müller H. S. P. et al., 2007, Phys. Chem. Chem. Phys., 9, 1579
Müller H. S. P., Brünken S., 2005, J. Mol. Spectrosc., 232, 213
Müller H. S. P., Thorwirth S., Roth D. A., Winnewisser G., 2001, A&A, 370, L49
Müller H. S. P., Schlöder F., Stutzki J., Winnewisser G., 2005, J Mol. Struct., 742, 215
NCBI, 2024, Ionization Energy in the Periodic Table of Elements, https://pubchem.ncbi.nlm.nih.gov/periodic-table/ionization-energy
Nguyen Luong Q. et al., 2011, A&A, 529, A41
Nicolaes D., Groenewegen M. A. T., Royer P., Lombaert R., Danilovich T., Decin L., 2018, A&A, 618, A143
Olofsson H., Eriksson K., Gustafsson B., Carlstrom U., 1993, ApJS, 87, 267
Olofsson H. et al., 2022, A&A, 665, A82
Plane J. M. C., Rajasekhar B., Bartolotti L., 1989, J. Chem. Phys., 91, 6177
Price S. D., Murdock T. L., 1983, AFGL-TR-0208 Environemental Research papers, 161, 0
Quintana-Lacaci G. et al., 2016, ApJ, 818, 192
Quintana-Lacaci G., Velilla-Prieto L., Agúndez M., Fonfría J. P., Cernicharo J., Decin L., Castro-Carrizo A., 2023, A&A, 669, A56
Renzini A., 1981, in Iben I., Renzini A.eds, Physical Processes in Red Giants. Springer Netherlands, Dordrecht, p. 431
Saberi M., Vlemmings W. H. T., De Beck E., 2019, A&A, 625, A81
Saberi M., Khouri T., Velilla-Prieto L., Fonfría J. P., Vlemmings W. H. T., Wedemeyer S., 2022, A&A, 663, A54
Sahai R., Scibelli S., Morris M. R., 2016, ApJ, 827, 92
Samus' N. N., Kazarovets E. V., Durlevich O. V., Kireeva N. N., Pastukhova E. N., 2017, Astron. Rep., 61, 80
Sánchez Contreras C., Bujarrabal V., Neri R., Alcolea J., 2000, A&A, 357, 651
Sánchez Contreras C., Alcolea J., Bujarrabal V., Castro-Carrizo A., Velilla Prieto L., Santand er-García M., Quintana-Lacaci G., Cernicharo J., 2018, A&A, 618, A164
Sánchez Contreras C., Alcolea J., Rodríguez Cardoso R., Bujarrabal V., Castro-Carrizo A., Quintana-Lacaci G., Velilla-Prieto L., Santander-García M., 2022, A&A, 665, A88
Saral G. et al., 2017, ApJ, 839, 108
Schöier F. L., Bast J., Olofsson H., Lindqvist M., 2007, A&A, 473, 871
Siebert M. A., Van de Sande M., Millar T. J., Remijan A. J., 2022, ApJ, 941, 90
Singh A. P., Edwards J. L., Ziurys L. M., 2022, AJ, 164, 230
Stoehr F. et al., 2017, The Messenger, 167, 2
Usov V. V., 1991, MNRAS, 252, 49
Van de Sande M., Decin L., Lombaert R., Khouri T., de Koter A., Wyrowski F., De Nutte R., Homan W., 2018, A&A, 609, A63
Van de Sande M., Millar T. J., 2022, MNRAS, 510, 1204
Van de Sande M., Walsh C., Millar T. J., 2023, Faraday Discuss., 245, 586
Velilla Prieto L. et al., 2017, A&A, 597, A25
Ventura P., Karakas A., Dell'Agli F., García-Hernández D. A., Guzman-Ramirez L., 2018, MNRAS, 475, 2282
Virtanen P. et al., 2020, Nat. Methods, 17, 261
Viti S., Caselli P., Hartquist T. W., Williams D. A., 2001, A&A, 370, 1017
Vlemmings W. H. T. et al., 2018, A&A, 613, L4
Wallström S. H. J. et al., 2024, A&A, 681, A50
Winnewisser G., Belov S. P., Klaus T., Schieder R., 1997, J. Mol. Spectrosc., 184, 468
Xu J.-L., Wang J.-J., 2013, MNRAS, 431, 2385
Zhang B. et al., 2014, ApJ, 781, 89

APPENDIX A: ADDITIONAL TABLES AND PLOTS

In this section, we present additional tables and plots which provide additional details of our observations. Table A1 provides details of the ALMA line observations and Table A2 provides details of the continuum images. Additional continuum images, with a focus on the Band 3 data, are shown in Fig. A1. The molecular line IDs are given in Table A3 and the full spectra are shown in Fig. A2 for the Band 6 spectra (with one spectral window given in Fig. 2) and in Fig. A3 for the Band 6 spectra.

The additional figures in this section are supplemental to the results presented in the body of the paper. In Fig. A4, we show some examples of soft parabola fits, as were discussed in Section 2.5. Figs A5 and A6 present channel maps of the CO emission as respectively observed with the extended array configuration in Band 6 and with Band 3. Fig. A7 shows the channel maps of the brightest observed SO_2 line, which is discussed in Section 3.4. In Fig. A8, we give a *PV* diagram of the NS line detected in Band 3, discussed in Section 3.5, and in Fig. A9, we present the population diagrams of $Na^{35}Cl$ and $K^{35}Cl$, as discussed in Section 3.6.

APPENDIX B: INTERSTELLAR CONTAMINATION

Here, we discuss in more detail the interstellar contamination experienced by OH 30.1−0.7 (see also Section 2.4), which we believe arises from the background star-forming region W43. Contamination can be seen in most previous studies of CO towards this object (e.g. De Beck et al. 2010), most of which rely on single-dish observations. Although some clever observational techniques can be employed to improve the single-dish observations of contaminated stars (see for example Heske et al. 1990), these are generally less precise than the spatial filtering of an interferometer.

In Fig. B1, we plot the combined ALMA spectra of CO $J = 2-1$, extracted for two apertures of different size, superposed with the spectra of the same line observed with the Atacama Pathfinder EXperiment (APEX, Güsten et al. 2006), the James Clerk Maxwell Telescope (JCMT), and the Institut de Radioastronomie Millimétrique (IRAM) 30-m telescope. The JCMT spectrum was first published in De Beck et al. (2010), the IRAM spectrum was first published in Justtanont et al. (2013), and the APEX spectrum is previously unpublished and was observed by the APEX/PI230

Table A1. Parameters of Band 3 and Band 6 ALMA observations for OH 30.1−0.7 from project 2016.1.00005.S.

Band, configuration	Frequencies [GHz]	Restoring beam [arcsec]	Beam PA [°]	Channel separation [km s^{-1}]	[MHz]	MRS[a] [arcsec]	Date observed
Band 3	100.028–101.899	1.756 × 1.179	−56.0	2.88	0.98	15.0	2016-12-05
Band 3	101.830–103.701	1.731 × 1.155	−55.7	2.83	0.98	15.0	2016-12-05
Band 3	111.947–113.818	1.576 × 1.078	−54.6	2.62	0.98	15.0	2016-12-05
Band 3	113.827–115.698	1.535 × 1.059	−54.9	2.57	0.98	15.0	2016-12-05
Band 6, extended	226.086–227.957	0.390 × 0.265	−67.2	2.57	1.95	4.5	2017-05-05
Band 6, compact	226.086–227.957	1.714 × 1.500	−76.6	2.57	1.95	12.8	2017-03-28
Band 6, combined	226.090–227.957	0.412 × 0.277	−67.1	2.57	1.95	–	–
Band 6, extended	229.085–230.956	0.395 × 0.256	−78.4	2.54	1.95	4.5	2017-05-05
Band 6, compact	229.085–230.956	1.711 × 1.480	−75.8	2.54	1.95	12.8	2017-03-28
Band 6, combined	229.089–230.956	0.427 × 0.273	−78.0	2.54	1.95	–	–
Band 6, extended	242.073–243.944	0.355 × 0.255	−73.5	2.42	1.95	4.5	2017-05-05
Band 6, compact	242.073–243.943	1.626 × 1.397	−75.9	2.42	1.95	12.8	2017-03-28
Band 6, combined	242.073–243.940	0.379 × 0.269	−73.1	2.42	1.95	–	–
Band 6, extended	244.086–245.957	0.373 × 0.251	−78.0	2.40	1.95	4.5	2017-05-05
Band 6, compact	244.086–245.957	1.617 × 1.384	−76.2	2.40	1.95	12.8	2017-03-28
Band 6, combined	244.086–245.953	0.401 × 0.265	−78.6	2.40	1.95	–	–

Note. [a] MRS is the maximum recoverable scale.

Table A2. Parameters of continuum images of OH 30.1−0.7 constructed from the observations of project 2016.1.00005.S.

Band, configuration	Restoring beam [arcsec]	Beam PA [°]	Rms [mJy beam^{-1}]	Peak flux [mJy beam^{-1}]	Dynamic range
Band 3	1.661 × 1.105	−55.9	1.27×10^{-2}	0.746	59
Band 3, resolution matching Band 6, compact	1.630 × 1.400	−75.0	1.34×10^{-2}	0.788	59
Band 6, extended	0.372 × 0.239	−71.7	1.40×10^{-2}	5.22	372
Band 6, compact	1.628 × 1.399	−75.0	4.21×10^{-2}	7.26	172
Band 6, combined, full resolution	0.397 × 0.252	−71.6	1.41×10^{-2}	5.26	374
Band 6, combined, taper = 0.5	0.662 × 0.536	−88.3	1.51×10^{-2}	6.47	427
Band 6, combined, taper = 0.8	0.986 × 0.829	−87.7	1.78×10^{-2}	7.19	403

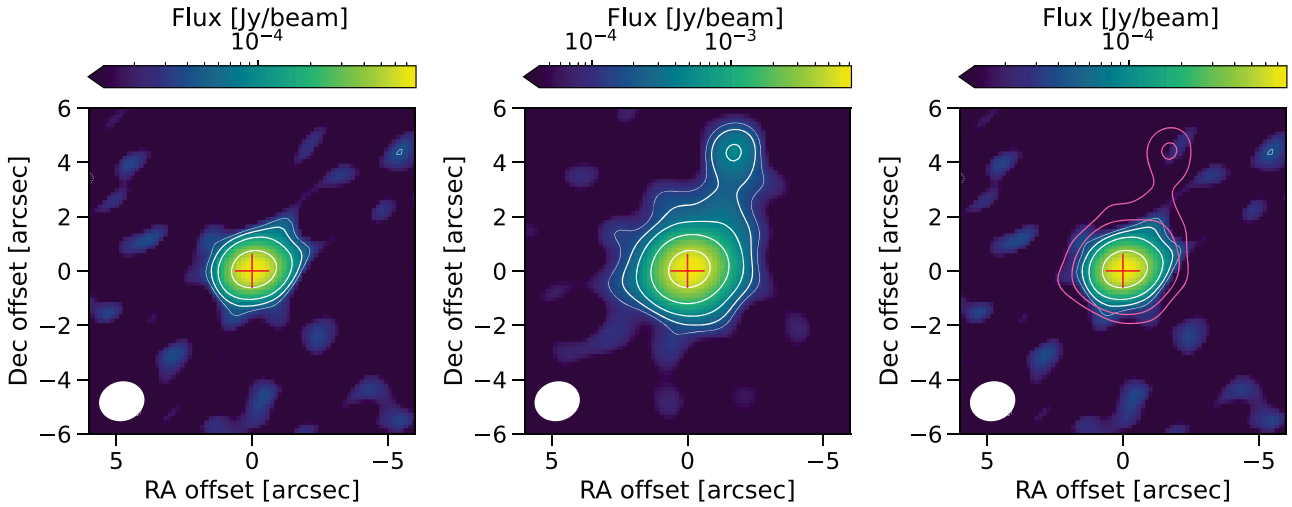

Figure A1. The continuum plots for OH 30.1−0.7 observed with ALMA Band 3 (left) and the compact configuration of ALMA Band 6 (centre), plotted on a logarithmic flux scale. The Band 3 image has been convolve to have the same beam as the Band 6 image. The contours indicate levels of 3σ (thinnest white line), and 5σ, 10σ, 30σ, and 100σ (thicker white lines). On the right, we plot the Band 3 continuum with the 5σ and 10σ contours of the compact Band 6 continuum overplotted in pink. In all panels, the crosses at (0,0) indicate the continuum peak. The beams are shown as white ellipses in the bottom-left corners. North is up and east is left.

instrument[2] in 2018 August (project ID: O-0102.F-9301B). There is considerable contamination in the JCMT observation, especially below velocities of around 107 km s^{-1}. The effect is even larger for the APEX observation, which has a larger HPBW ($\theta = 27$ arcsec for APEX and $\theta = 20$ arcsec for JCMT). IRAM, which has the smallest beam ($\theta = 10.7$ arcsec), suffers from the least amount of contamination, but the contamination still impacts the flux below ~ 107 km s^{-1}. In Fig. B1, we adjust the flux axis of the left panel to best show the CO emission originating from OH 30.1−0.7, while the middle panel shows the full range of the emission/absorption detected by APEX and JCMT. The contamination entirely dominates the APEX and JCMT flux below 100 km s^{-1}. Nevertheless, the ALMA observations are in general agreement with the single-dish observations above 107 km s^{-1}, suggesting that the AGB flux is likely not resolved out at those velocities in the Band 6 observations. The fact that the ALMA spectra extracted for two apertures of different sizes (radii of 8 and 3 arcsec) largely agree with each other indicates that the CO flux is mostly confined within 3 arcsec of the continuum peak. We also checked the line profile of the ALMA observations taken with only the extended array configuration, and found that the flux (for an extraction aperture with diameter 6 arcsec) does not deviate from that of the combined data; i.e. even for the extended configuration, there is no resolved-out flux (see also the extended configuration channel maps in Fig. A5). Based on these comparisons, and considering that CO is the most extended observed molecule, we assert that none of the Band 6 observations suffer from resolved-out flux.

We also compare the ALMA Band 3 CO $J = 1 - 0$ line with the IRAM observation of the same line first published in Justtanont et al. (2013), plotted in the right panel of Fig. B1. Since the single-dish beam is larger at the lower frequency, the IRAM line suffers from significant contamination. The Band 3 observation has a larger maximum resolvable scale than the Band 6 observation, and hence is also more susceptible to contamination. From inspecting the channel maps, shown in Fig. A6, we can see significant contamination, in the form of diagonal bars, in the channels with velocities below 100 km s^{-1}. The contamination can also be seen as spikes in the full spectrum in Fig. A3 and contributes to a difficulty in disentangling a possible $K^{35}Cl$ $v = 0$ line from both the AGB CO emission and the background contamination (see Table A3). However, given the shape of the CO emission and the larger maximum resolvable scale for the Band 3 data, we also assume that there is no resolved-out flux in the Band 3 observations.

[2]PI230 is a collaboration between the European Southern Observatory (ESO) and the Max-Planck-Institut für Radioastronomie (MPIfR).

APPENDIX C: COMPARISON WITH PREVIOUS STUDIES OF MOLECULAR DETECTIONS AND DISTRIBUTIONS

C1 SiS

SiS is a commonly observed molecule that has been detected in the envelopes of all chemical types of AGB stars. It is generally found to be more abundant in carbon-rich CSEs than oxygen-rich CSEs (Schöier et al. 2007). However, Danilovich et al. (2018) found that SiS was more likely to be detected for AGB stars with higher mass-loss rates and hence denser CSEs, across chemical types. This trend was confirmed by Massalkhi, Agúndez & Cernicharo (2019) for a larger sample of carbon stars, although Danilovich et al. (2019) also found that very sensitive ALMA observations could detect low abundances of SiS (down to $\sim 10^{-8}$ relative to H_2) for even low mass-loss rate oxygen-rich stars. Since OH 30.1−0.7 is thought to have a high mass-loss rate, detections of SiS are expected where the lines are covered by our observations.

Table A3. Lines identified towards OH 30.1−0.7. Spectra are shown in Figs A2 and A3.

Species	Freq [GHz]	E_{low} [K]	Transition	υ_{cent} [km s^{-1}]	υ_{w} [km s^{-1}]	Flux [Jy km s^{-1}]	Ap.[a] [arcsec]	Notes
SO_2	100.878	7.8	$v = 0, J_{K_a,K_c} = 2_{2,0} - 3_{1,3}$	99.3	18.9	0.32	3.0	
$Na^{37}Cl$	101.962	17.1	$v = 0, J = 8 - 7$	100.2	19.0	0.24	2.0	
$^{34}SO_2$	102.032	2.7	$v = 0, J_{K_a,K_c} = 3_{1,3} - 2_{0,2}$	99.9	19.0	0.40	3.0	
$^{33}SO_2$	102.998	2.8	$v = 0, J_{K_a,K_c} = 3_{1,3} - 2_{0,2}$	...	...	...	...	Tentative and hyperfine
$Na^{35}Cl$	103.415	537.4	$v = 1, J = 8 - 7$	103.7	12.0	0.06	2.0	
$C^{17}O$	112.359	0.0	$v = 0, J = 1 - 0$	...	...	...	...	Tentative
$Na^{37}Cl$	114.701	22.0	$v = 0, J = 9 - 8$	99.4	23.2	0.19	1.0	
NS	115.154	3.3	$^2\Pi_{1/2}, v = 0, e,\ J = 5/2 - 3/2,\ F = 7/2 - 5/2$	...	...	...	...	Brightest hyperfine component
NS	115.157	3.3	$^2\Pi_{1/2}, v = 0, e,\ J = 5/2 - 3/2,\ F = 5/2 - 3/2$	...	...	...	...	Hyperfine
NS	115.163	3.3	$^2\Pi_{1/2}, v = 0, e,\ J = 5/2 - 3/2,\ F = 3/2 - 1/2$	...	...	...	...	Hyperfine
CO	115.271	0.0	$v = 0, J = 1 - 0$	100.9	17.0	48.20	5.0	
$K^{35}Cl$	115.292	38.8	$v = 0, J = 15 - 14$	...	...	...	...	Blend with CO; tentative
NS	115.556	3.4	$^2\Pi_{1/2}, v = 0, f,\ J = 5/2 - 3/2,\ F = 5/2 - 3/1$	...	...	...	...	Brightest hyperfine, tentative
NS	115.571	3.4	$^2\Pi_{1/2}, v = 0, f,\ J = 5/2 - 3/2,\ F = 5/2 - 3/2$	...	...	...	...	Hyperfine, tentative
NS	115.572	3.3	$^2\Pi_{1/2}, v = 0, f,\ J = 5/2 - 3/2,\ F = 3/2 - 1/2$	...	...	...	...	Hyperfine, tentative
SO_2	226.300	108.2	$v = 0, J_{K_a,K_c} = 14_{3,11} - 14_{2,12}$	99.2	19.0	0.79	2.0	
^{30}SiS	226.502	1118.2	$v = 1, J = 13 - 12$	99.7	11.7	0.05	0.3	
$Na^{35}Cl$	227.351	2143.1	$v = 4, J = 18 - 17$	101.2	7.6	0.05	0.5	
$K^{35}Cl$	227.497	954.4	$v = 2, J = 30 - 29$	100.3	7.0	0.07	0.5	
$Na^{37}Cl$	227.560	607.5	$v = 1, J = 18 - 17$	101.8	12.6	0.33	0.5	Blend with wing of ^{30}SiS
^{30}SiS	227.590	65.6	$v = 0, J = 13 - 12$	99.8	22.0	1.04	1.0	Blend with wing of $Na^{37}Cl$
$Na^{37}Cl$	229.246	93.6	$v = 0, J = 18 - 17$	100.2	18.1	1.11	1.0	
$Si^{34}S$	229.501	66.1	$v = 0, J = 13 - 12$	98.7	22.8	1.34	1.0	
$^{41}K^{35}Cl$	229.682	952.3	$v = 2, J = 31 - 30$	98.6	14.6	0.06	0.3	
$K^{37}Cl$	229.819	559.6	$v = 1, J = 31 - 30$	100.6	9.5	0.07	0.5	
$^{34}SO_2$	229.858	7.6	$v = 0, J_{K_a,K_c} = 4_{2,2} - 3_{1,3}$	99.9	22.6	1.54	3.0	
$K^{35}Cl$	230.321	160.5	$v = 0, J = 30 - 29$	101.6	13.4	0.36	0.5	
^{29}SiS	230.510	1128.6	$v = 1, J = 13 - 12$	...	...	...	...	Blend with wing of CO
CO	230.538	5.5	$v = 0, J = 2 - 1$	101.9	17.9	214.50	5.0	
$Na^{35}Cl$	230.779	1129.3	$v = 2, J = 18 - 17$	101.2	11.8	0.31	0.5	
$^{29}Si^{34}S$	242.478	75.7	$v = 0, J = 14 - 13$	...	...	...	...	
$K^{35}Cl$	242.612	976.6	$v = 2, J = 32 - 31$	100.5	14.8	0.12	0.5	
SO_2	243.088	41.4	$v = 0, J_{K_a,K_c} = 5_{4,2} - 6_{3,3}$	...	...	...	...	Tentative. Blend with $K^{37}Cl$
$K^{37}Cl$	243.110	971.5	$v = 2, J = 33 - 32$	...	...	...	...	Blend with SO_2
$Na^{35}Cl$	243.574	1140.4	$v = 2, J = 19 - 18$	101.5	11.4	0.34	0.5	
^{30}SiS	243.917	1129.1	$v = 1, J = 14 - 13$	100.2	6.2	0.07	0.3	
SO_2	244.254	82.2	$v = 0, J_{K_a,K_c} = 14_{0,14} - 13_{1,13}$	98.7	21.7	5.38	3.0	
$^{41}K^{35}Cl$	244.448	974.7	$v = 2, J = 33 - 32$	...	...	...	...	Tentative
$^{34}SO_2$	244.482	81.9	$v = 0, J_{K_a,K_c} = 14_{0,14} - 13_{1,13}$	...	...	...	...	Tentative
$K^{37}Cl$	244.594	582.1	$v = 1, J = 33 - 32$	100.6	8.0	0.03	0.3	
CS	244.936	23.5	$v = 0, J = 5 - 4$	99.39	18.2	1.95	3.0	
^{30}SiS	245.088	76.5	$v = 0, J = 14 - 13$	99.3	19.6	1.10	1.0	
$^{34}SO_2$	245.302	28.9	$v = 0, J_{K_a,K_c} = 6_{3,3} - 6_{2,4}$	...	...	...	...	Tentative
$Na^{35}Cl$	245.401	626.2	$v = 1, J = 19 - 18$	101.3	14.6	0.77	0.5	
SO_2	245.563	61.0	$v = 0, J_{K_a,K_c} = 10_{3,7} - 10_{2,8}$	98.3	19.7	2.79	3.0	
$K^{35}Cl$	245.624	183.0	$v = 0, J = 32 - 31$	101.9	12.2	0.34	0.5	
$Si^{34}S$	245.960	1134.2	$v = 1, J = 14 - 13$	99.7	7.7	0.07	0.5	

Notes. For NS, we list the three brightest hyperfine components (see discussion in Section 3.5). For $C^{17}O$, we give the frequency and quantum numbers corresponding to the brightest hyperfine component, which happens to also be the central hyperfine component. [a]Ap. gives the radius of the circular aperture used to extract the spectrum from which the central velocity (υ_{cent}), velocity width (υ_{w}) and integrated flux were calculated. These line parameters were not calculated for known blended lines or lines that were too marginal in the spectra to fit a soft parabola function (see the text for details).

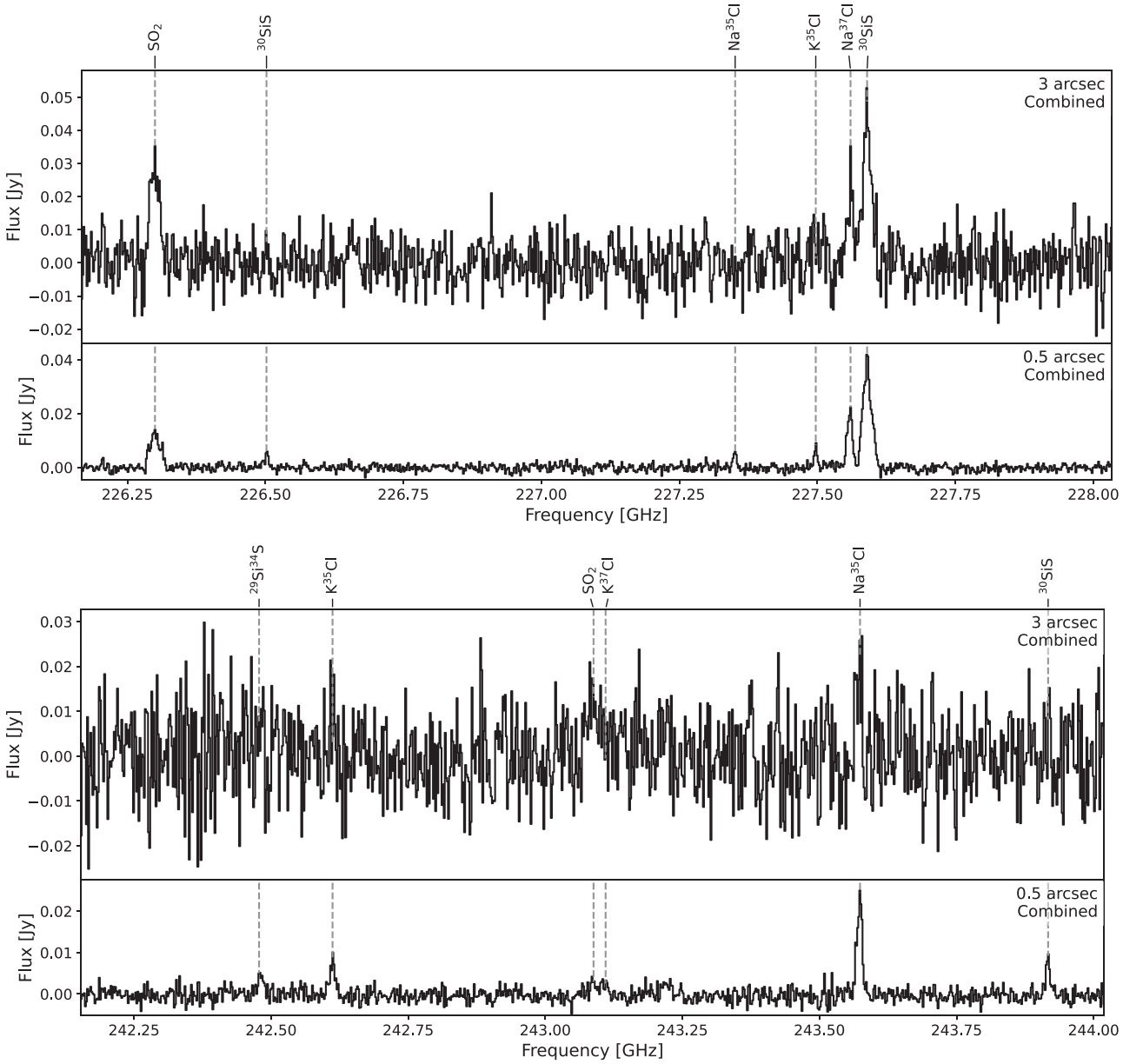

Figure A2. ALMA Band 6 spectra for OH 30.1−0.7. For each spectral window, we show spectra for a large extraction aperture and a small extraction aperture, with the extraction aperture radius and ALMA configuration given in the top right of each subplot. The molecular carriers of various spectral lines are indicated at the top of each plot. See Table A3 for details.

C2 CS

Since it is a carbon-bearing molecule, CS has often been associated with carbon-rich CSEs. However, it has also been detected in several oxygen-rich CSEs, as well as towards S-type AGB stars (e.g. Lindqvist et al. 1988; Danilovich et al. 2018). Similar to SiS, CS has been found to be more prevalent in higher density oxygen-rich and S-type CSEs (Danilovich et al. 2018), possibly because of a higher prevalence of shocks (e.g. from larger pulsations in Mira variables as compared with semi-regular variables) in these CSEs which can liberate C from CO to enable the formation of CS. This may also result in CS being more abundant for Mira variable stars than semi-regular variable stars, among the oxygen-rich AGBs (Danilovich et al. 2019). However, for carbon-rich AGB stars, the abundance of CS has generally been found to be one to two orders of magnitude higher than for oxygen-rich stars (Danilovich et al. 2018; Massalkhi et al. 2019). Since OH 30.1−0.7 has a high mass-loss rate and hence high wind density, detections of CS are expected despite it being an oxygen-rich star.

C3 SO_2

SO_2 is thought to be formed in CSEs from SO. Previous studies, mostly focusing on AGB stars known to have low initial masses, have shown that the distributions of SO and SO_2 can be divided into two groups of morphological structures in AGB CSEs. Danilovich et al. (2016) found, from a small sample, that SO distributions could either be centred on the star or could exhibit a shell-like distribution, with the relative abundance of SO peaking further out in the CSE, rather than being centred on the star. It was

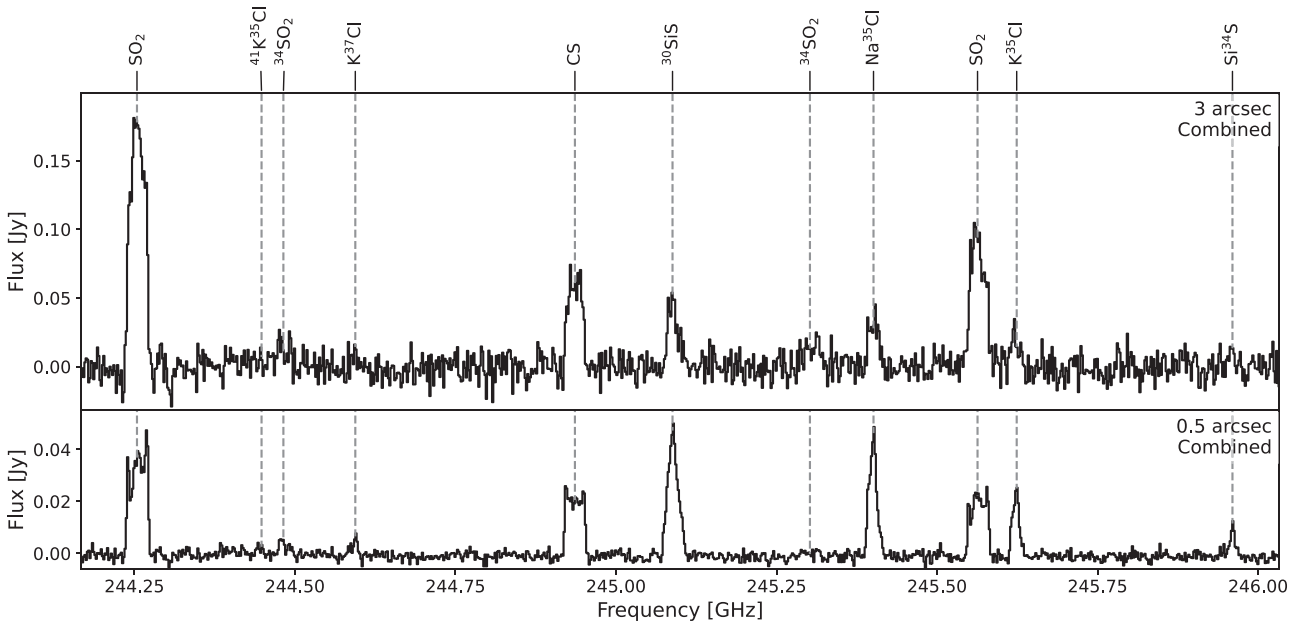

Figure A2. – *continued*.

found that the stars with lower mass-loss rates (or lower wind densities) exhibited centralized SO distributions, while stars with higher mass-loss rates (or higher wind densities) exhibited shell-like SO distributions. The larger ATOMIUM survey, using spatially resolved ALMA observations, confirmed this trend for SO and also for SO_2 (Wallström et al. 2024). Earlier data had been insufficient to determine the spatial distribution of SO_2. The chemical models of Van de Sande & Millar (2022) and Van de Sande, Walsh & Millar (2023) predict more shell-like SO and SO_2 distributions for AGB stars with UV-producing companions and/or with more clumpy CSEs.

C4 NS

Aside from the AGB stars discussed in Section 4.1.1, NS has been detected towards an early planetary nebula (Sánchez Contreras et al. 2000), giant molecular clouds (where it seen to be enhanced in massive star-forming regions such as Orion KL, McGonagle & Irvine 1997), hot cores (Xu & Wang 2013), comets (e.g. Irvine et al. 2000), and a starburst galaxy (Martín et al. 2003, 2021). All of these objects contain regions with high UV fluxes (or experience UV flux during part of their orbits, in the case of comets), suggesting that this could be the dominant formation mechanism of astronomical NS. Viti et al. (2001) performed chemical models of shocks in hot cores and found that NS can be enhanced through shock heating, which is broadly similar to the UV-driven chemistry driving the NS formation around W Aql (Van de Sande & Millar 2022; Danilovich et al. 2024). Older chemical models, which do not consider shocks or enhanced UV chemistry were not able to reproduce the observed abundances of NS in hot cores by several orders of magnitude (e.g. Millar & Herbst 1990).

C5 Chlorides

The first astronomical detections of NaCl and KCl were reported by Cernicharo & Guelin (1987) towards the nearby carbon-rich AGB star CW Leo (along with AlCl). Subsequently, abundances relative to H_2 of 1.8×10^{-9} for NaCl and $\sim 5 \times 10^{-10}$ for KCl were derived from more comprehensive observations by Agúndez et al. (2012), who also found the $^{35}Cl/^{37}Cl$ isotopic ratio to be 2.9 ± 0.3, close to the solar isotopic value of 3.3 ± 0.3. Spatially resolved observations by Quintana-Lacaci et al. (2016) found elongated NaCl and KCl emission and concluded that the NaCl was likely arranged in a spiral or torus (with the formation of such a structure likely driven by a companion). That study also detected NaCl in the first vibrationally excited state for the first time.

NaCl has also been detected towards a handful of oxygen-rich stars. The low-mass AGB star IK Tau (initial mass ~ 1.3 $M_\odot$, Danilovich et al. 2017a) has been observed to exhibit several different rotational lines of NaCl in the ground vibrational state (Milam et al. 2007; Velilla Prieto et al. 2017). Spatially resolved observations with ALMA found it to have clumpy irregular NaCl ($v = 0$) emission (Decin et al. 2018). A subsequent 3D analysis by Coenegrachts et al. (2023) found that the emission was roughly arranged in a clumpy spiral and the formation of NaCl may have been driven by a stellar or planetary companion. We note that the nearby low-mass AGB star R Dor – observed with the same spectral setup and sensitivity as IK Tau but not presently thought to have a solar type binary companion (Vlemmings et al. 2018) – did not have any detections of NaCl (or NS, Decin et al. 2018). Additional detections of NaCl and KCl were reported by Wallström et al. (2024) in the ATOMIUM survey for the AGB stars IRC-10529 (NaCl in $v = 0$, 1 and KCl in $v = 0$), IRC + 10011 (NaCl in $v = 0$, 1, 2 and KCl in $v = 0$) and GY Aql (NaCl in $v = 0$). All three of these oxygen-rich AGB stars are thought to have companions shaping their winds, though the precise natures of these companions are not yet known (Decin et al. 2020). The RSGs VY CMa, NML Cyg, and VX Sgr also have NaCl detected towards them (Milam et al. 2007; Kamiński et al. 2013; Decin et al. 2016; Singh, Edwards & Ziurys 2022; Quintana-Lacaci et al. 2023; Wallström et al. 2024). In the spatially resolved observations of VY CMa, NaCl is seen to trace high-velocity jets (Quintana-Lacaci et al. 2023).

There have also been detections of NaCl towards early post-AGB stars, such as CRL 2688 (the Egg Nebula, Highberger et al. 2003)

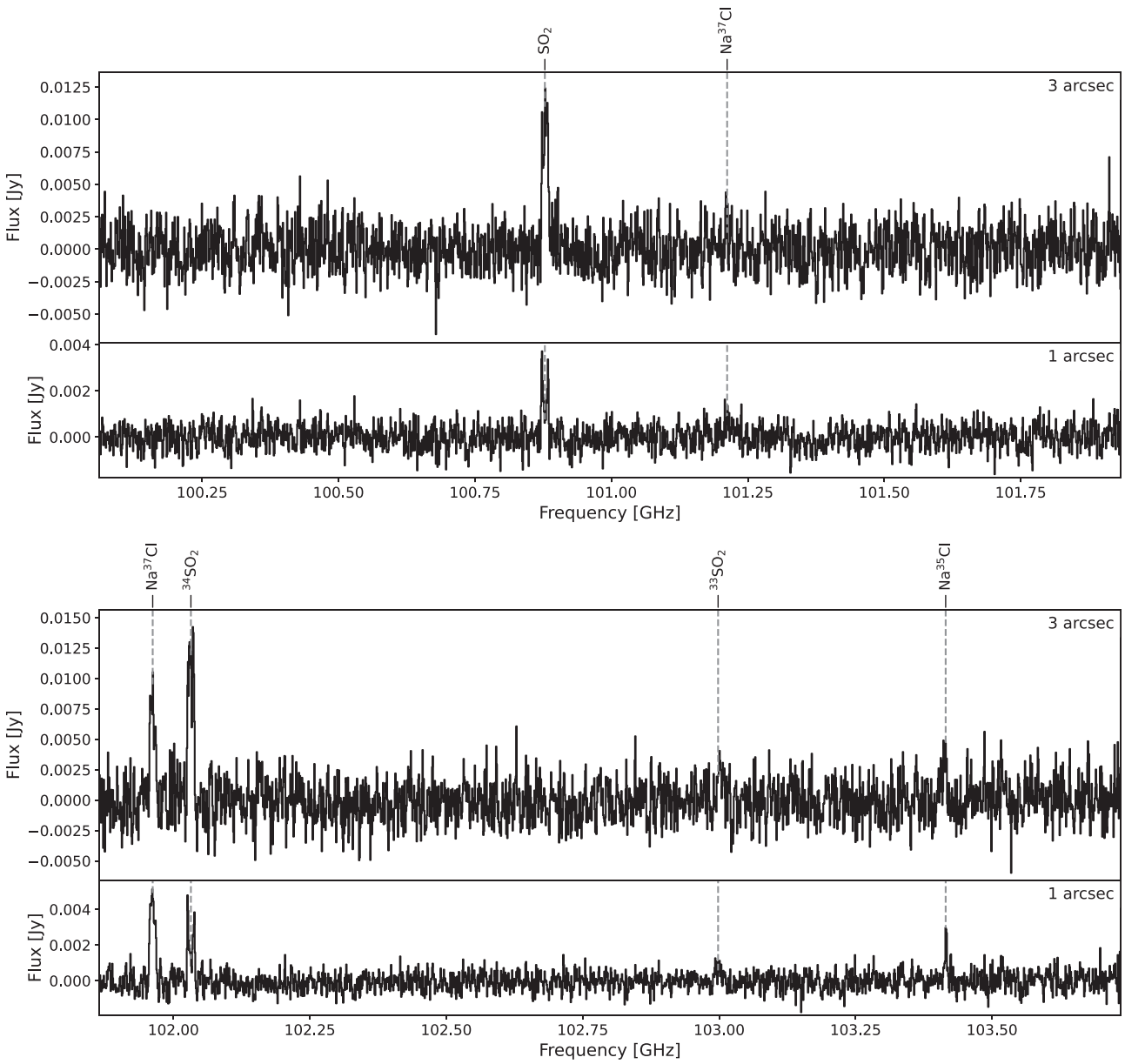

Figure A3. ALMA Band 3 spectra for OH 30.1−0.7. For each spectral window, we show spectra for a large extraction aperture and a small extraction aperture, with the extraction aperture radius in the top right of each subplot. The molecular carriers of various spectral lines are indicated at the top of each plot. See Table A3 for details.

and OH 231.8+4.2 (the Rotten Egg Nebula, Sánchez Contreras et al. 2018, 2022), both of which have bipolar outflows, with NaCl detected in shell-like structures. Highberger et al. (2003) used the IRAM 30-m telescope to detect several NaCl lines in the ground vibrational state towards CRL 2688. They suggest that the formation of NaCl is likely driven by shocks and clumping in the high-velocity outflows. Sánchez Contreras et al. (2022) used ALMA to observe OH 231.8+4.2, an AGB star which seems to be undergoing a premature evolution into the pre-Planetary Nebula phase, possibly driven by the A0 companion on a relatively close orbit (20 au). They detect vibrationally excited NaCl up to $v = 2$ (and tentatively $v = 3$) and KCl (up to $v = 1$) in a rotating and expanding cylindrical structure around the central star, coinciding with a circumbinary dust disc. They also find a relatively high vibrational temperature ($T_{\rm vib} = 1125 \pm 160$ K), consistent with NaCl forming in hot conditions. In this case the dust disc could also shield the Na and K atoms, preventing excessive photoionization. Sánchez Contreras et al. (2022) conclude that NaCl and KCl are good tracers of high-density regions and may be shock tracers. While OH 30.1−0.7 may have a similar companion to OH 231.8+4.2, it clearly does not have a bipolar outflow (and is not easily detected in the optical, unlike the Rotten Egg Nebula), suggesting a different orbital configuration.

Another astrophysical environment in which NaCl and KCl have been frequently detected are high-mass young stellar objects (Ginsburg et al. 2019, 2023). Dubbed 'binaries' because of the strong correlation between NaCl and H_2O detections, Ginsburg et al. (2023) found that the salt detections were neither rare nor ubiquitous. They also find that the NaCl emission is restricted to the relatively inner regions of discs or outflows, which are likely to be

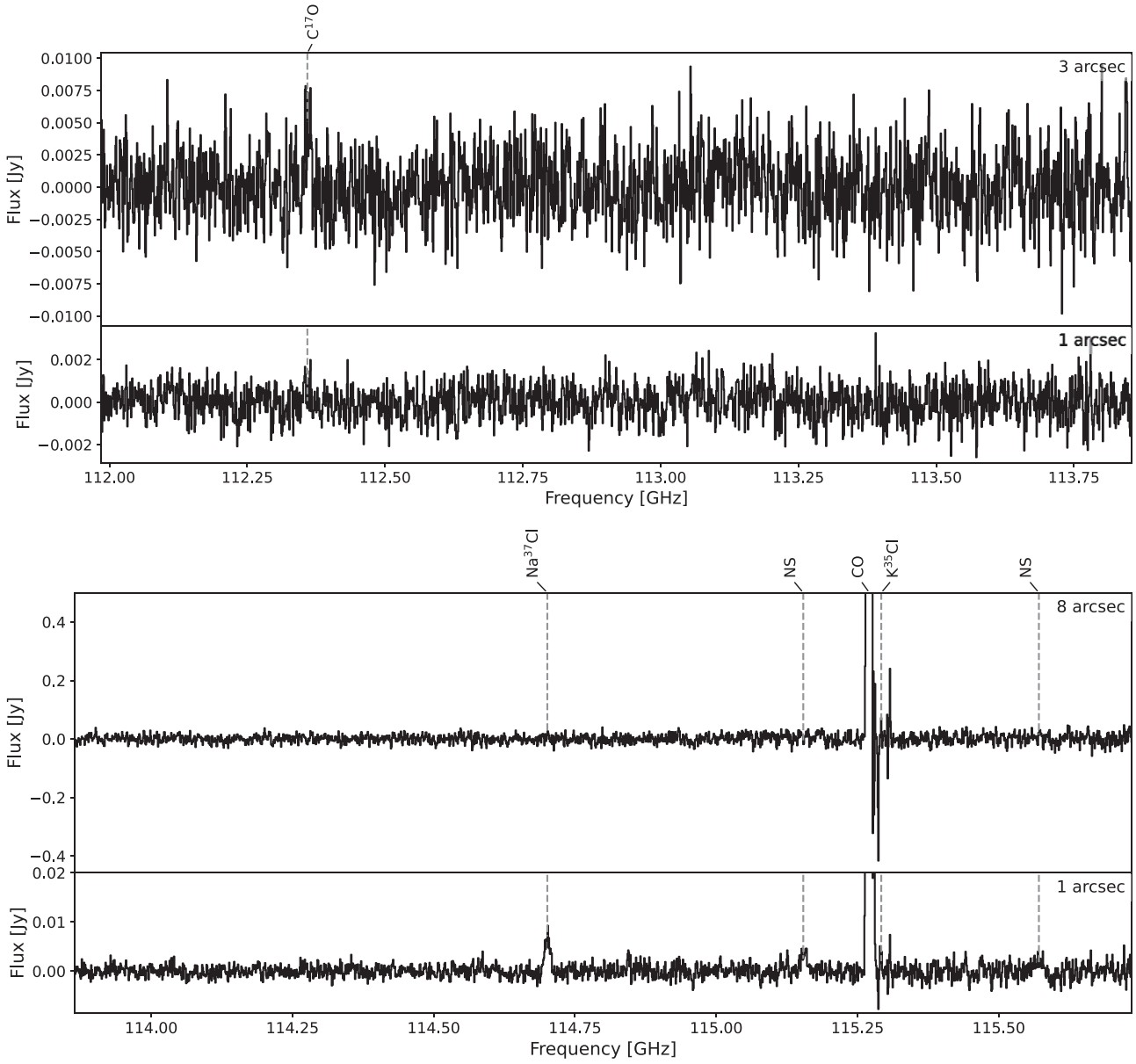

Figure A3. – *continued*.

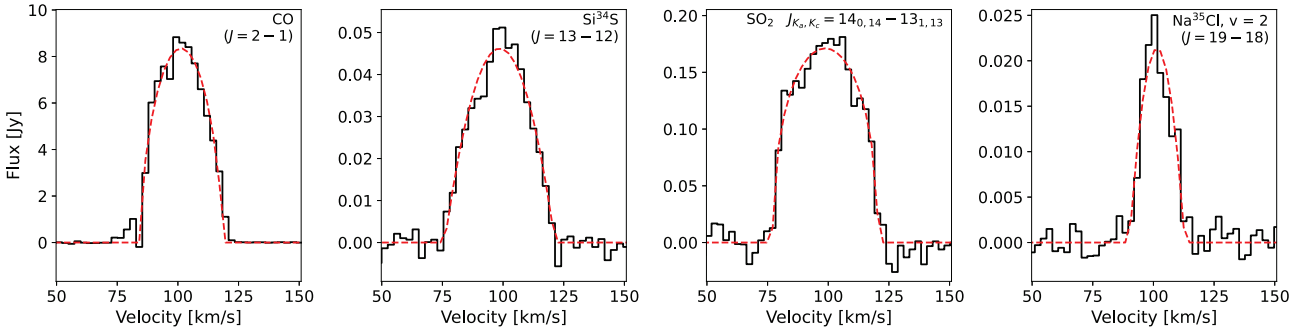

Figure A4. Examples of soft parabola fits to selected lines towards OH 30.1−0.7. Data are plotted as black histograms and the fits are shown as dashed red lines. The molecular carriers and the corresponding transitions are given in the top-right corner of each panel. Further details for each line, including the extraction aperture for the spectrum, are given in Table A3. Details of the fitting procedure are given in Section 2.5.

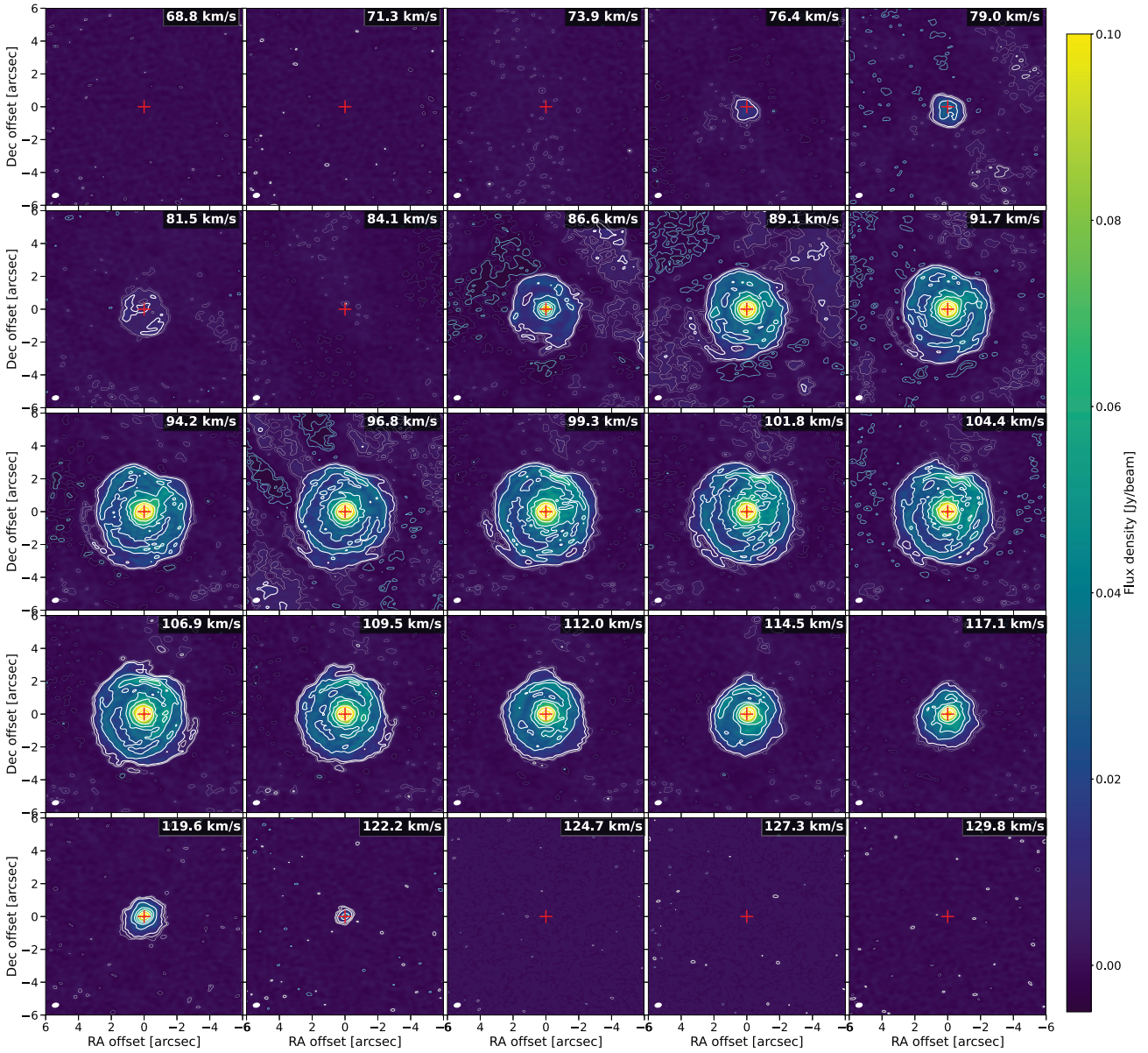

Figure A5. Channel maps for CO $J = 2 - 1$ towards OH 30.1−0.7, as observed with the more extended ALMA configuration. The thicker white contours are drawn at levels of 10σ, 30σ, 50σ, 70σ, 100σ, 150σ, 200σ, 300σ, and 500σ, the thinner grey contours at levels of 3σ and 5σ, and the dashed cyan contours at levels of -3σ and -5σ. The cross at (0,0) indicates the position of the continuum peak. The velocity of each channel is shown in the top-right corner of each panel and the beam is shown as a white ellipse in the bottom-left corners. North is up and east is left. Note that although some interstellar contamination has been resolved out by ALMA, a significant amount remains, especially for channels with velocities lower than 100 km s^{-1}.

the warmer (but not ionized) regions of their sources. This is broadly similar to the centrally confined NaCl and KCl detected here for OH 30.1−0.7, and likely correspond to similar hot and shocked formation conditions.

C5.1 The formation of NaCl and KCl

The main formation pathway for NaCl and KCl is thought to be through neutral–neutral reactions between the alkali metal atom and HCl. The reaction for NaCl has a relatively high activation energy of 42 kJ mol^{-1} (Husain & Marshall 1986; Plane, Rajasekhar & Bartolotti 1989), significantly more than the 12 kJ mol^{-1} barrier for K+HCl (Helmer & Plane 1993). Thus, formation of NaCl and KCl is favoured at higher temperatures. Furthermore, both reactions are endothermic (by 19.2 and 7.8 kJ mol^{-1}, respectively), and the reverse reactions of NaCl and KCl with H are fast with small temperature dependences. This means that NaCl and KCl can only persist if the H density is relatively low (see below). Another important consideration is that Na and K have low ionization potentials (5.139 eV for Na, 4.341 eV for K, NCBI 2024, which correspond to wavelengths of 241 and 286 nm, respectively) and their singly ionized states, Na^+ and K^+, are unreactive closed shell ions. This means that UV photons from a hot star could easily ionize Na

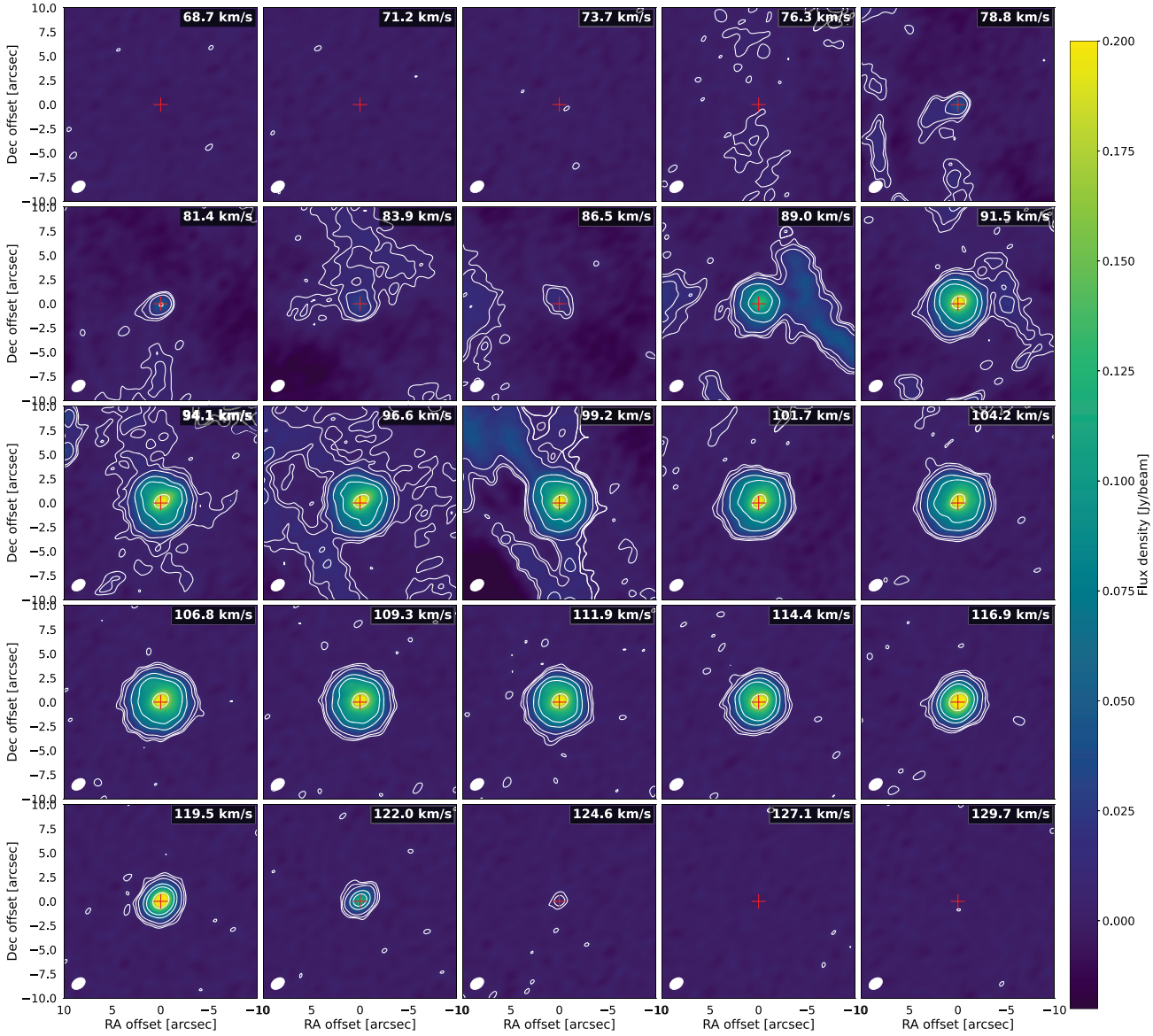

Figure A6. Channel maps for CO $J = 1 - 0$ towards OH 30.1−0.7. The contours are drawn at levels of 3σ, 5σ, 10σ, 30σ, 50σ, and 100σ and the cross at (0,0) indicates the position of the continuum peak. The velocity of each channel is shown in the top-right corner of each panel and the beam is shown as a white ellipse in the bottom-left corners. North is up and east is left. Note that there is significant interstellar contamination for channels with velocities lower than 100 km s^{-1}.

and K and subsequent ion-neutral reactions would not readily occur, hence effectively removing Na and K and preventing the formation of their chlorides. This dilemma is avoided if the environment is dense enough to provide shielding against ionization. Given the thick, dusty envelope of OH 30.1−0.7 (see Section 4.2 and Marini et al. 2023) and its high mass-loss rate, there should be an extremely high amount of extinction in the inner wind, which would strongly attenuate any UV photons except for in the immediate vicinity of the UV-producing star. For this reason, heating from UV photons alone is unlikely to drive the formation of NaCl or KCl since the UV photons will be highly attenuated and, if they were not, they would instead ionize the metals and prevent the formation of NaCl and KCl. Note that this is the opposite scenario to the formation of NS. NS forms after its precursor N_2 has been photodissociated (Van de Sande & Millar 2022; Danilovich et al. 2024), whereas NaCl and KCl require that their precursors Na and K not be photoionized. This difference could explain why the distributions of NaCl and NS in the Band 3 zeroth moment maps (Figs 10 and 9) are not colocated. An interesting additional check on the chemistry would be mapping the SiN emission (which was not covered in our observations) because its formation follows after the photoionization of Si to Si^+.

Another possible obstacle for the formation of NaCl and KCl is the H/H_2 ratio in the wind. If this is too high (e.g. if H/H_2 $\gtrsim 10^{-4}$) then the steady-state reactions will favour the formation of HCl, Na, and K, rather than NaCl and KCl. Given the observations presented here and the implied high abundances of both NaCl and KCl, we can confidently say that the H/H_2 ratio is low. High temperatures (e.g. 1000–2000 K) and high densities will also contribute to more rapid formation of NaCl and KCl (as all chemical reactions proceed more

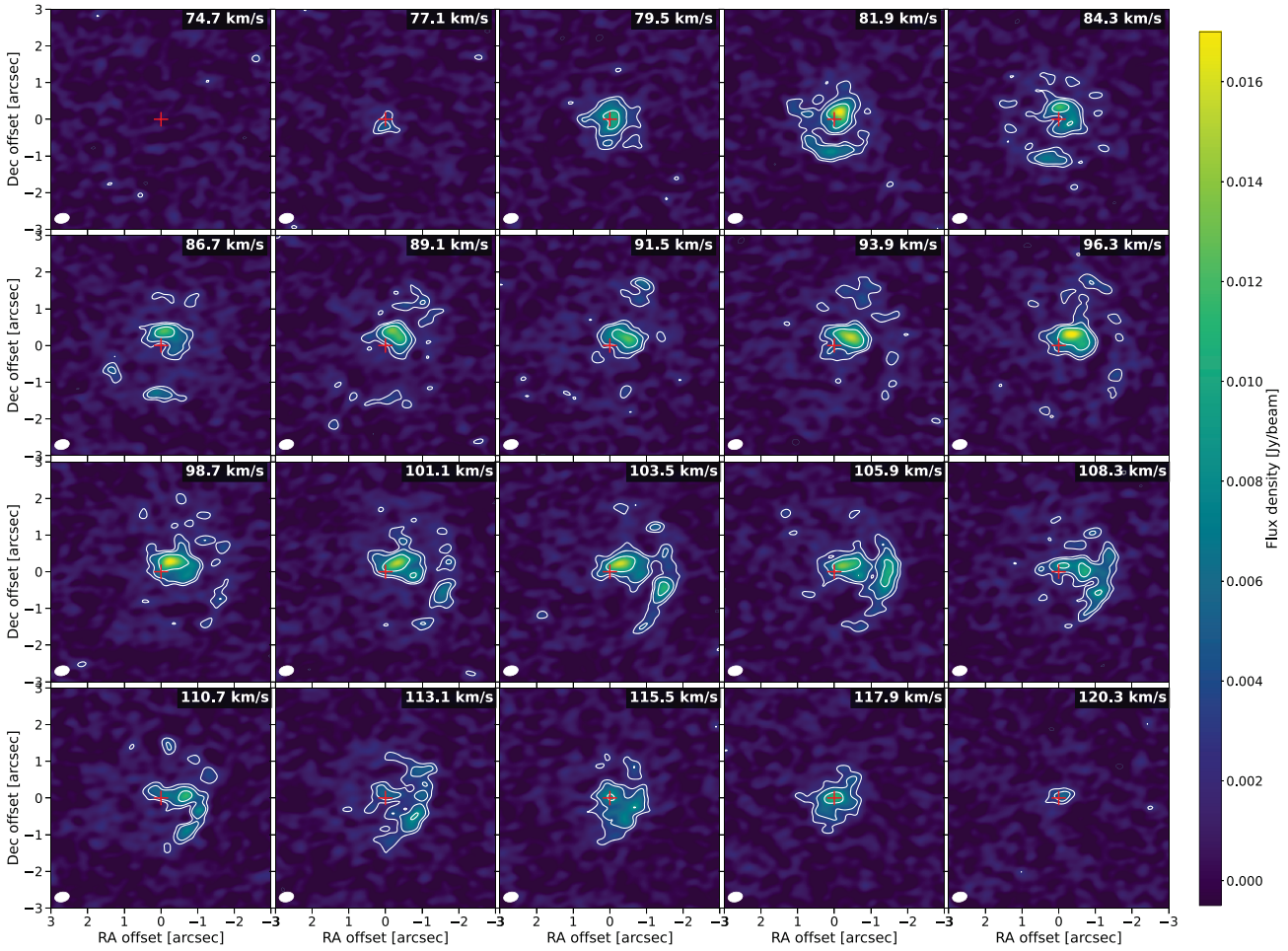

Figure A7. Channel maps for SO_2 $J_{K_a,K_c} = 14_{0,14} \rightarrow 13_{1,13}$ at 244.254 GHz towards OH 30.1−0.7. The contours are drawn at levels of 3σ, 5σ, and 10σ, and the cross at (0,0) indicates the position of the continuum peak. The velocity of each channel is shown in the top-right corner of each panel and the beam is shown as a white ellipse in the bottom-left corners. North is up and east is left.

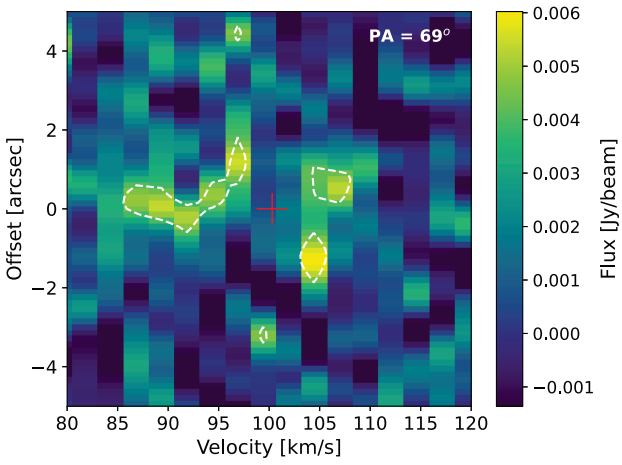

Figure A8. *PV* diagram for NS *e* towards OH 30.1−0.7. The diagram was constructed for line passing through the continuum peak at an angle of 69° east from north (as shown in Fig. 9). The contours are drawn at levels of 3σ and the red cross at (100.3,0) indicates the position and systemic velocity of the AGB star.

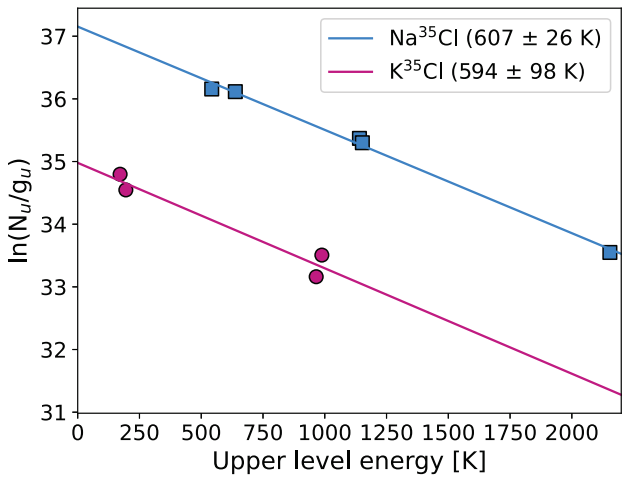

Figure A9. Population diagrams for $Na^{35}Cl$ (blue squares) and $K^{35}Cl$ (pink circles). The lines give the best linear fit to the data. Average gas temperatures are given in the legend and are close to 600 K for both molecules. The source-averaged column densities are 1.4×10^{12} and 1.6×10^{11} cm^{-2} for $Na^{35}Cl$ and $K^{35}Cl$, respectively.

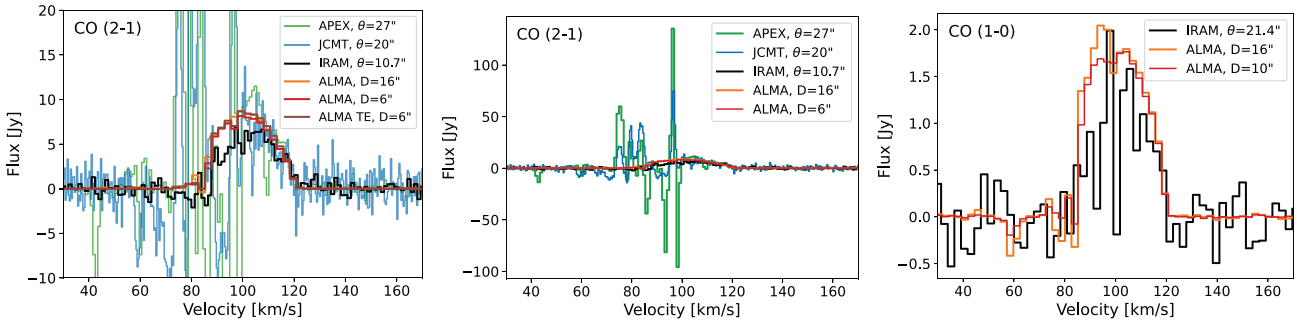

Figure B1. ALMA observations of CO towards OH 30.1−0.7 compared with APEX, JCMT, and IRAM 30-m observations of the same lines. The legends give the HPBW, θ, for the single-dish data, and the diameter of the circular extraction apertures, D, for the ALMA data. TE refers to data observed with only the ALMA extended configuration. The single-dish observations show significant line contamination from sources other than the AGB stars. The left and middle panels show CO ($J = 2 - 1$) with the left panel having a flux scale that allows the CO emission to be clearly seen, while the middle panel has a flux scale that shows the full range of the ISM contamination at velocities $\lesssim 100$ km s^{-1}. The right panel shows CO ($J = 1 - 0$).

rapidly at higher number densities). This fits with previous results finding that NaCl is preferentially formed as a consequence of shocks (Cherchneff 2012).

C6 Species not detected or not covered

Some of the species that we might expect to see towards a star such as OH 30.1−0.7 were either not covered in our observations or were not detected. To eliminate confusion between these two possibilities, we briefly summarize here which key molecular species were not detected and which were not covered.

SiO and HCN are both seen almost ubiquitously towards AGB stars of all types. Our spectral set up was such that no lines in the ground or first four vibrationally excited states of ^{28}Si^{16}O, ^{29}Si^{16}O, or ^{30}Si^{16}O were covered. No lines of HCN or H^{13}CN in the ground vibrational state were covered. Transitions of CN, the photodissociation product of HCN, were covered but not detected above the noise.

SO is generally observed towards the same stars as SO_2, with similar distribution patterns in the CSEs (Danilovich et al. 2016; Wallström et al. 2024). Although we present several detections of SO_2 towards OH 30.1−0.7, no lines of SO or its isotopologues (^{32}SO, ^{34}SO, or ^{33}SO) were covered in our observations.

The recent work of Baudry et al. (2023) identified several highly excited H_2O lines (with upper level energies in the range 3954–9012 K) in ALMA observations of a sample of oxygen-rich AGB and RSG stars. Unfortunately, none of the emission lines detected in the Baudry et al. (2023) sample were covered in our spectral configurations. We found no other lines of H_2O towards OH 30.1−0.7, despite clear detections of relatively low-energy H_2O lines observed by *Herschel*/HIFI (Justtanont et al. 2015). No OH lines in the ground vibrational state were covered in the Band 6 data.

H_2S is associated with high mass-loss rate/high CSE density oxygen-rich AGB stars (Danilovich et al. 2017b). Only two lines of H_2S were covered in our observations and both were high-energy lines ($E_{\rm low} > 2000$ K) that have not previously been detected for any AGB stars. One lower energy line of $H_2{}^{34}S$ was covered ($E_{\rm low} = 240$ K) but not detected.

Despite our detections of NaCl and KCl, Al^{35}Cl was not detected. However, the only line in the ground vibrational state of Al^{35}Cl fell in the less sensitive Band 3 data and could be blended with $^{34}SO_2$. In the case of Al^{37}Cl, one line in the ground vibrational state fell in each of the Band 3 and 6 observations. Neither is detected above the noise.

AlF, which was detected alongside AlCl towards W Aql (Danilovich et al. 2021) and has been seen towards various oxygen-rich AGB stars (Saberi et al. 2022; Wallström et al. 2024), was not detected towards OH 30.1−0.7. This is despite a line in the ground vibrational state being covered by our Band 6 observations. The chemistry behind AlF is not yet fully understood (see Danilovich et al. 2021, for a more extended discussion), but it seems to not be directly linked to the other metal halides (i.e. NaCl and KCl) that are so conclusively detected towards OH 30.1−0.7.

SiN and SiC were identified by Van de Sande & Millar (2022) as tracers of a UV-emitting companion star, along with NS. Although NS was detected for OH 30.1−0.7, SiN was not covered in our observations, and two lines of SiC were covered in Band 6 but not detected above the noise.

APPENDIX D: PREVIOUS OBSERVATIONAL STUDIES OF OH 30.1−0.7

The study of rotational CO lines towards OH 30.1−0.7 has been hampered by contamination along its line of sight, as discussed in Section 2.4 (see also De Beck et al. 2010), mainly originating from the massive star-forming region W43, located around 1.6 kpc behind OH 30.1−0.7. The observations taken with APEX and JCMT shown in Fig. B1 are too contaminated to allow any meaningful study of the star and, indeed, a determination of the mass-loss rate was not carried out by De Beck et al. (2010) for this reason. The IRAM 30-m telescope has a smaller HPBW and hence appears to suffer less from ISM contamination, especially for the CO $J = 2 - 1$ line, but it is clear from our ALMA observations, especially from inspection of the channel maps (Fig. 3 and Fig. A6) that there is unavoidable contamination directly along the line of sight to OH 30.1−0.7. Even though a lot of this is resolved out by ALMA, some elements of the contaminating molecular cloud cannot be avoided owing to the small angular sizes of dense elements, comparable in size to the OH 30.1−0.7 CO envelope extent. Giant molecular clouds are generally expected to be relatively cold, so they are brighter in the lower energy CO transitions. However, massive star-forming clumps have

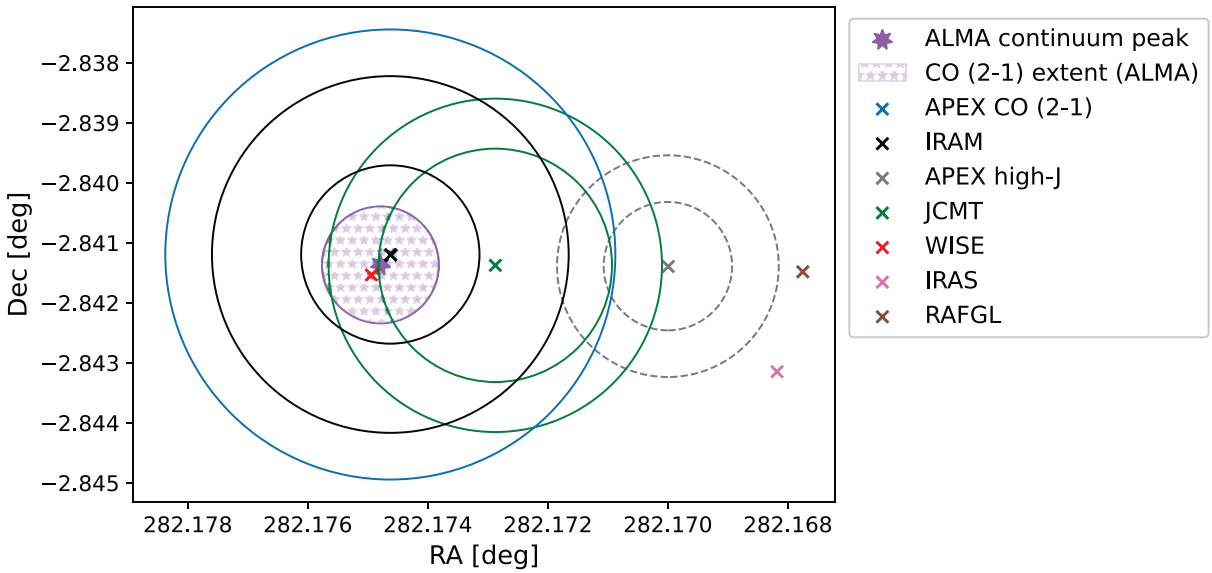

Figure D1. Location on the sky of OH 30.1−0.7 and the pointings of various observations targeting the star. The continuum peak based on our observations is plotted as a purple star and a purple shaded circular region with a radius of 3.5 arcsec represents the extent of the CO $J = 2 - 1$ (see Fig. 3). The coordinates and HPBW of various other observations are also plotted (see the text for references). Note that the centres of the APEX CO (2−1) and IRAM beams are at the same coordinates, as are the HIFI observations, the large beams for which are not plotted. Not shown are the coordinates given in the *WISE*, *ISO*, and GCVS catalogues, which are all within ~ 1 arcsec of the ALMA continuum peak.

been shown to also exhibit high-J CO lines (e.g. Hoang et al. 2023). Without spatially resolved observations for all studied CO transitions, we cannot completely rule out contamination in any CO towards OH 30.1−0.7.

D1 Forensic astronomy

Through a careful examination of past catalogues and other observations of OH 30.1−0.7, we have determined that there has historically been some uncertainty in the precise position of this star. Our ALMA continuum observations are of high astrometric accuracy (see Table 1) and represent the best measured position for OH 30.1−0.7. Some examples of past uncertainties are detailed below.

The study of Justtanont et al. (2013) included the IRAM observations shown in Fig. B1 and two higher energy CO lines observed with APEX, $J = 7 - 6$ and $J = 4 - 3$. Both of these higher energy lines were not detected above the noise but also do not exhibit significant contamination, which is somewhat perplexing, since the $J = 9 - 8$ and $J = 5 - 4$ lines were clearly detected by *Herschel*/HIFI (with some possible contamination seen in $J = 5 - 4$, see fig. 10 in Justtanont et al. 2013).

To investigate this conundrum we checked the original observations discussed above and plot the HPBW and right ascension and declination (RA and Dec.) of these observations in Fig. D1. We also checked various catalogues and past observations for the coordinates listed for OH 30.1−0.7 and compared them with the RA and Dec. we find for the continuum peak in this work (based on the Band 6 extended continuum, see Table 1). The majority of the listed coordinates for this star fall within $\lesssim 1$ arcsec of our continuum peak, including those from the *Wide-field Infrared Survey Explorer* (*WISE*, Cutri et al. 2012), the General Catalogue of Variable Stars (GCVS 5.1, Samus' et al. 2017), the *Infrared Space Observatory* (*ISO*, Kessler et al. 1996) and from the aforementioned IRAM, HIFI (Justtanont et al. 2013), and APEX ($J = 2 - 1$, this work, ID: O-0102.F-9301B) observations. The JCMT CO $J = 2 - 1$ and $J = 3 - 2$ observations (De Beck et al. 2010) are offset from the ALMA continuum peak by about 7 arcsec, meaning that the telescope beam at $J = 2 - 1$ mostly covers the extent of the emission observed with ALMA, but the smaller $J = 3 - 2$ misses a significant portion of the AGB emission.

This is illustrated in Fig. D1, where we approximate the ALMA CO emission as a circle of radius 3.5 arcsec centred on the continuum peak and plot various telescope beams and their pointings. The relatively small APEX beams covering the CO $J = 4 - 3$ and $J = 7 - 6$ lines are centred on a point ~ 17 arcsec from the ALMA continuum peak and, as shown in Fig. D1, do not overlap with the CO envelope at all.

We also note that some older catalogues, such as the *Infrared Astronomical Satellite* (*IRAS*, Helou & Walker 1988) and the Revised Air Force Geophysical Laboratory Infrared Sky Survey (RAFGL, Price & Murdock 1983), list coordinates even more significantly offset from our continuum peak (by ~ 25 arcsec for both *IRAS* and RAFGL), most likely owing to resolution limitations. The coordinates listed in the study of Heske et al. (1990), discussed in Section 4.2.1, agree with our position to within 0.33 arcsec.

This paper has been typeset from a TEX/LATEX file prepared by the author.